# Physics Based Simulations of Reynolds Number Effects in Vortex Intensive Incompressible Flows

**K. Sreenivas, D. Hyams, B. Mitchell, L. Taylor, W.R. Briley, D.L. Whitfield**
Computational Simulation and Design Center, P.O. Box 9627
Mississippi State, MS 39762, USA

## Abstract

The primary objective of this study is to study the differences in the computed flow fields between model-, quarter- and full-scale Reynolds numbers. Towards this end, an efficient RANS incompressible flow solver, **U$^2$NCLE**, capable of performing viscous, high Reynolds number flow simulations for complex geometries using unstructured grids has been developed. This flow solver is to be demonstrated for large-scale meshes with good sub-layer resolution ($y^+ < 1$) and approximately $10^6$ points or more with an emphasis toward hydrodynamic applications. Results are shown for model-, quarter- and full-scale computations on the SUBOFF model with sail at various angles of drift. Effects of grid density on computed flow fields at model- and full-scale Reynolds numbers are also considered.

## Introduction

The accurate computation of forces and moments is of paramount importance in the computation of the maneuvering response of a vehicle. The dynamic forces acting on a vehicle can be broken down into inertial (pressure) and viscous components. Typically, for low angles of attack (drift), the flow is not separated and inertial forces dominate. For such cases, good agreement with experimental data can be achieved using potential flow or Euler codes. For the higher angles of attack (drift), the flow is turbulent and is characterized by large-scale boundary layer separation. Consequently, the viscous effects are important and it becomes essential to use a Navier-Stokes code to correctly model the physics and thus obtain good agreement with experimental data.

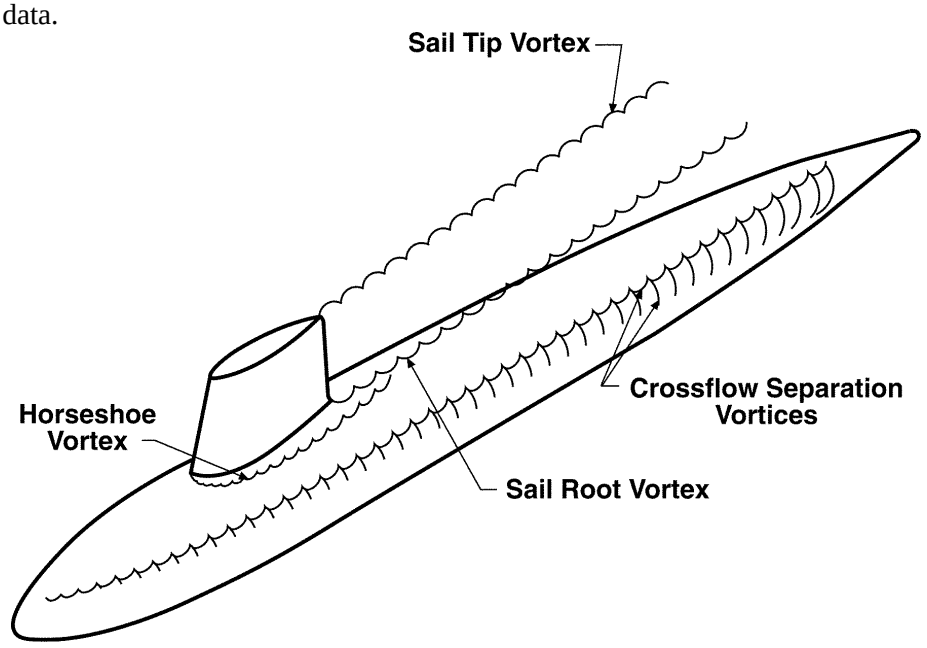


**Figure 1: Schematic of the complex flow-field for a submarine**

*Paper presented at the RTO AVT Symposium on "Advanced Flow Management: Part A – Vortex Flows and High Angle of Attack for Military Vehicles", held in Loen, Norway, 7-11 May 2001, and published in RTO-MP-069(I).*

# Report Documentation Page

*Form Approved*
*OMB No. 0704-0188*



| 1. REPORT DATE | 2. REPORT TYPE | 3. DATES COVERED |
|---|---|---|
| **00 MAR 2003** | **N/A** | **-** |

| 4. TITLE AND SUBTITLE | 5a. CONTRACT NUMBER |
|---|---|
| **Physics Based Simulation of Renolds Number Effects in Vortex Intensive Incompressible Flows** | 5b. GRANT NUMBER |
| | 5c. PROGRAM ELEMENT NUMBER |
| 6. AUTHOR(S) | 5d. PROJECT NUMBER |
| | 5e. TASK NUMBER |
| | 5f. WORK UNIT NUMBER |
| 7. PERFORMING ORGANIZATION NAME(S) AND ADDRESS(ES) **NATO Research and Technology Organisation BP 25, 7 Rue Ancelle, F-92201 Neuilly-Sue-Seine Cedex, France** | 8. PERFORMING ORGANIZATION REPORT NUMBER |
| 9. SPONSORING/MONITORING AGENCY NAME(S) AND ADDRESS(ES) | 10. SPONSOR/MONITOR'S ACRONYM(S) |
| | 11. SPONSOR/MONITOR'S REPORT NUMBER(S) |

12. DISTRIBUTION/AVAILABILITY STATEMENT
**Approved for public release, distribution unlimited**

13. SUPPLEMENTARY NOTES
**Also see: ADM001490, Presented at RTO Applied Vehicle Technology Panel (AVT) Symposium held inLeon, Norway on 7-11 May 2001, The original document contains color images.**

14. ABSTRACT

15. SUBJECT TERMS

| 16. SECURITY CLASSIFICATION OF: | | | 17. LIMITATION OF ABSTRACT | 18. NUMBER OF PAGES | 19a. NAME OF RESPONSIBLE PERSON |
|---|---|---|---|---|---|
| a. REPORT | b. ABSTRACT | c. THIS PAGE | | | |
| **unclassified** | **unclassified** | **unclassified** | **UU** | **14** | |

Figure 1 illustrates the complex nature of the flow-field for a submarine with sail. The flow field is dominated by vortical type flow separation. Some of the structures that can be seen in the schematic are: (1) the horseshoe vortices (2) the sail root vortex (3) the sail tip vortex and (4) cross-flow separation vortices. (1) and (2) are the result of junction flows (similar to a wing-body junction in an aircraft) and (3) is similar to a wing tip vortex. The flow past the submarine is characterized by the significant interaction between the horseshoe and the root vortices. At moderate to high angles of drift, the flow is dominated by cross-flow separation. Prediction of this phenomenon is vital for accurate force and moment computations.

An understanding of Reynolds number effects is essential for extrapolating model- or quarter-scale results to full-scale. The state-of-the-art in the prediction of full-scale maneuvering performance utilizes a combination of experience, heuristics, and empiricism. To better understand these scale effects, it would be ideal to validate the flow solver at full-scale Reynolds numbers. However, the preponderance of experimental data available for undersea vehicles is limited to model-scale. The unavailability of full-scale data prevents a thorough validation of the high Reynolds number capabilities, but, basic validation can be achieved using flat plate boundary layer results and Reynolds number scaling.

The remainder of this paper is organized as follows: The governing equations are addressed in the first section. The second section presents an overview of the flow solver and briefly covers the parallelization aspects. The third section contains a brief overview of the method used to track the vortex cores and find their trajectories. The fourth section presents results that illustrate the high Reynolds number capabilities of the flow solver. Results are also presented that demonstrate the ability of the flow solver to accurately predict forces and moments for model-scale Reynolds numbers. The effect of grid point distribution on the computed flow-fields is also evaluated. Flow fields arising from model-, quarter- and full-scale Reynolds numbers are compared and the differences analyzed Finally, some conclusions are drawn and areas of current focus highlighted.

## Governing Equations

The unsteady three-dimensional incompressible Reynolds-averaged Navier-Stokes equations are presented here in Cartesian coordinates and in conservative form. Following [1], an artificial time derivative term ($\frac{\partial \rho_a}{\partial \tau}$, where $\rho_a = P/\beta$) has been added to the continuity equation to cast the complete set of governing equations into a time-marching form. The non-dimensional equations can be written in integral form as

$$\frac{\partial}{\partial t}\int_{\Omega} Q\, dV + \int_{\partial\Omega} \vec{F}.\hat{n}\, dA = \frac{1}{\mathrm{Re}}\int_{\partial\Omega} \vec{G}.\hat{n}\, dA$$

where $\hat{n}$ is the outward pointing unit normal to the control volume $\Omega$. The vector of dependent variables and the components of the inviscid and viscous fluxes are given as

$$Q = \begin{bmatrix} P \\ u \\ v \\ w \end{bmatrix}, \quad \vec{F}.\hat{n} = \begin{bmatrix} \beta\ (\Theta - a_t) \\ u\Theta + \hat{n}_x P \\ v\Theta + \hat{n}_y P \\ w\Theta + \hat{n}_z P \end{bmatrix}, \quad \text{and } \vec{G}\cdot\hat{n} = \begin{bmatrix} 0 \\ \hat{n}_x \tau_{xx} + \hat{n}_y \tau_{xy} + \hat{n}_z \tau_{xz} \\ \hat{n}_x \tau_{yx} + \hat{n}_y \tau_{yy} + \hat{n}_z \tau_{yz} \\ \hat{n}_x \tau_{zx} + \hat{n}_y \tau_{zy} + \hat{n}_z \tau_{zz} \end{bmatrix}$$

where $\beta$ is the artificial compressibility parameter (typically 15 in this work), *u*, *v*, and *w* are the Cartesian velocity components in the *x*, *y*, and *z* directions, and are the components of the

normalized control volume face vector. $\Theta$, the velocity normal to a control volume face, is defined as $\Theta = \hat{n}_x u + \hat{n}_y v + \hat{n}_z w + a_t$, where the grid speed $a_t = -(V_x \hat{n}_x + V_y \hat{n}_y + V_z \hat{n}_z)$. Note that $\vec{V_s} = V_x \hat{i} + V_y \hat{j} + V_z \hat{k}$ is the control volume face velocity. The variables in the preceding equations are non-dimensionalized using a characteristic length (*L*), and free-stream values of velocity $(U_\infty)$, density $(\rho_\infty)$, and viscosity $(\mu_\infty)$. Thus, Reynolds number is defined as $\frac{U_\infty L}{\nu_\infty}$. Pressure is normalized with $\frac{P^* - P_\infty}{\rho_\infty U_\infty^2}$, where $P^*$ is the local dimensional static pressure. The viscous stresses are $\tau_{ij} = (\mu + \mu_t)\left(\frac{\partial u_i}{\partial x_j} + \frac{\partial u_j}{\partial x_i}\right)$ where $\mu$ and $\mu_t$ are the molecular and eddy viscosities, respectively.

The two equation $q - \omega$ turbulence model is used for simulation of turbulent effects in high Reynolds number flows. This model uses a transport equation each for the velocity scale and length scale to specify the distribution of the eddy viscosity. The details of the implementation are available elsewhere in the literature [2] and will not be repeated here.

## Algorithm Details

The baseline flow solver, **U$^2$NCLE** (***U***nstructured ***Un***steady ***C***omputation of Fie***l***d ***E***quations), is a node-centered, finite volume, implicit scheme applied to general unstructured grids with nonsimplical elements. The flow variables are stored at the vertices and surface integrals are evaluated on the median dual surrounding each of these vertices. The non-overlapping control volumes formed by the median dual completely cover the domain, and form a mesh that is dual to the elemental grid. Thus, a one-to-one mapping exists between the edges of the original grid and the faces of the control volumes.

The solution algorithm consists of the following basic steps: reconstruction of the solution states at the control volume faces, evaluation of the flux integrals for each control volume, and the evolution of the solution in each control volume in time.

For quick turnaround time in a design environment, it is essential to parallelize the flow solution algorithm. The present parallel unstructured viscous flow solver is based on coarse-grained domain decomposition for concurrent solution within sub-domains assigned to multiple processors. The solution algorithm employs iterative solution of the implicit approximation, with the iteration hierarchy as shown in Figure 2. In addition, domain decomposition takes place with each node in the domain uniquely mapped to a given task. The code employs MPI message passing for inter-processor communication.

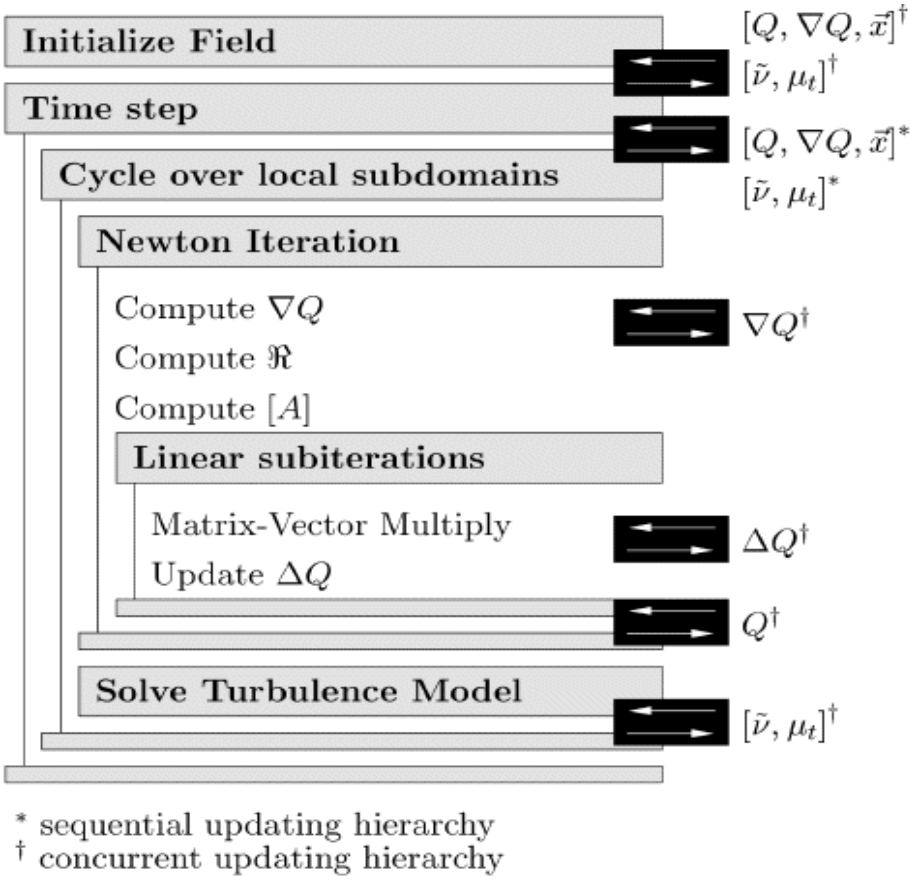


**Figure 2: Iteration Hierarchy**

## Vortex Tracking

The flow-field, as illustrated in Figure 1, consists of a variety of vortical structures. This poses an unique challenge in the sense that a method is required that will identify and track the vortices. The method employed in this study uses the so called intrinsic swirl parameter which identifies swirling regions in the flow-field by examining the eigenvalues of the physical velocity gradient tensor [3]. This method has been successfully employed to identify and track vortices [3][4]. The computation of intrinsic swirl can be broken down into the following major steps:

- Calculate the physical velocity gradient tensor $\nabla\vec{V}$.
- Determine if the eigenvalues of $\nabla\vec{V}$ are complex.
- Calculate the orbit time ($t_{orbit}$) from the imaginary component of the complex eigenvalue.
- Calculate the convection time ($t_{conv}$), based on the characteristic length and characteristic velocity (defined as the velocity in the plane whose normal is parallel to the real eigenvector).
- Define Intrinsic Swirl as $t = \dfrac{t_{conv}}{t_{orbit}}$.

Once the intrinsic swirl parameter has been computed for all points in the flow field, contour and iso-surfaces can be created from which vortex trajectories can be identified.

## Results

A key aspect of this work is to compare solutions obtained for model- and full-scale Reynolds numbers. To this end, the solver is used to compute turbulent flows over a flat plate at model- and full-scale Reynolds numbers. The comparison with theoretical data is shown in Figure 3. As can be seen, the agreement is good.

The SUBOFF model [5], which is representative of a generic underwater vehicle, is presented as the next candidate test case. The SUBOFF case is based on the model detailed in [5] with flow measurements taken from [6] and [7]. The configurations used in this study are the non-appended SUBOFF hull and the SUBOFF hull with sail.

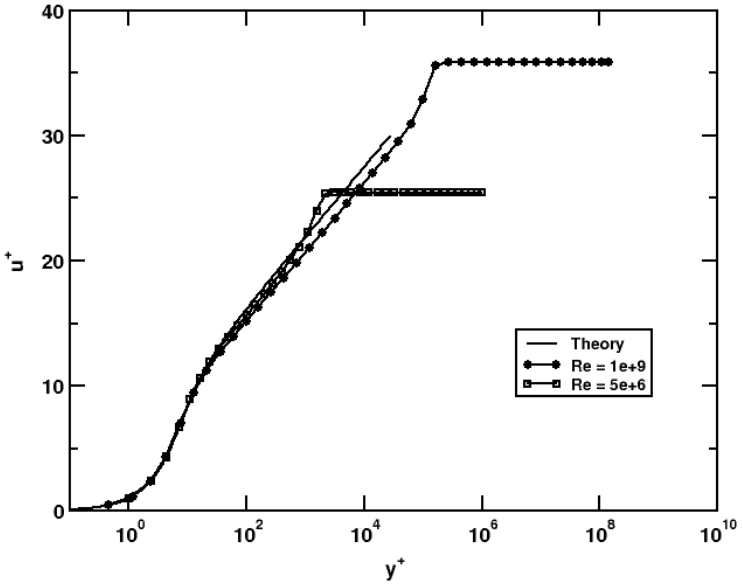


**Figure 3: Comparison of flat plate boundary layer profiles with theory**

## Non-Appended SUBOFF Hull

The next test case chosen for validation of the high Reynolds number capability of the code is the SUBOFF non-appended hull for which model-scale skin friction data is available [7]. The skin friction is computed at model (Re = 14 million), and full-scale (Re = 1.2 billion) Reynolds numbers. As shown in Figure 4, agreement between experiment and computation is excellent on the aft part of the hull (where measurements are available). The numerical results for the full-scale case have been subjected to a Reynolds number scaling [8] before comparison to the experimental data. Like the measurements, the computed skin friction coefficients display a definite peak where the flow accelerates (hull neck-down point, x/L ~ 0.77), and a decreasing $C_f$ as the flow slows between x/L = 0.8 to x/L = 0.95. The secondary peak at x/L = 0.98 is due to a small flow acceleration over the shoulder of the after-body cap.

The comparison between the full-scale and the Reynolds scaled model-scale skin friction shows some similarities, but significant differences can be observed too. This points to a need for simulation of the full-scale Reynolds number flow fields directly and to not rely on Reynolds scaling of model data to arrive at the full-scale behavior. The capability to robustly simulate full-scale Reynolds numbers is considered a key feature of the numerical algorithm presented here.

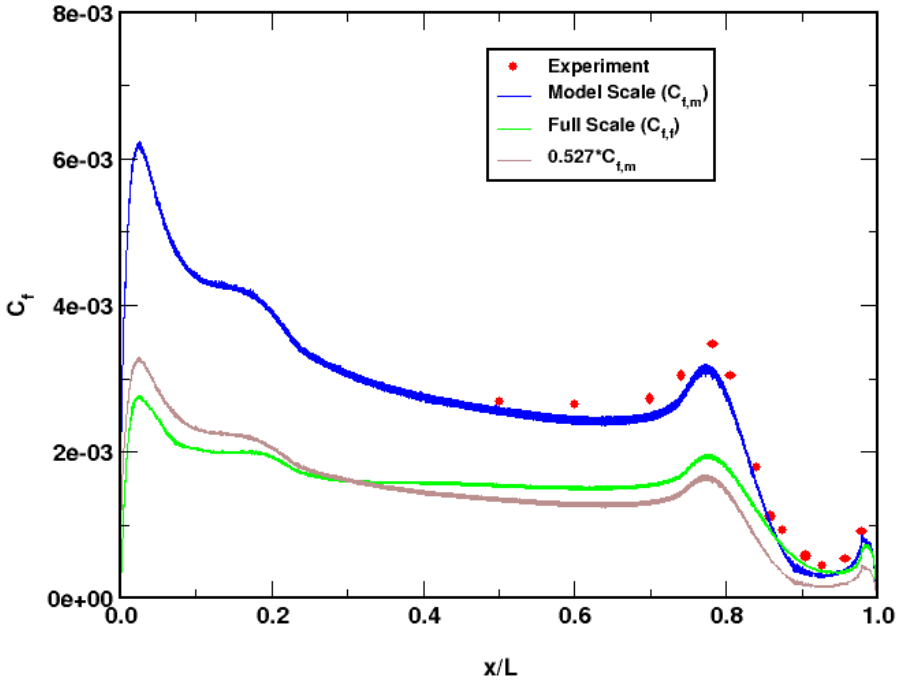


**Figure 4: Comparison of full- and model-scale computations for the non-appended SUBOFF hull**

## SUBOFF Hull with sail

The ability of the flow solver to predict the forces and moments accurately (model-scale) has been demonstrated by comparing forces and moments for the SUBOFF hull with stern appendages to experimental data in [9]. In this paper, comparisons are made for the SUBOFF hull with sail (Figure 5) for various angles of drift at a Reynolds number of 14 million. As can be seen from this figure, the agreement varies from good to excellent. The most significant difference is at the 16$^o$ angle of drift, where the flow-field is unsteady due to shedding from the sail tip. All computations presented here are steady, and no attempt was made to run the solver in an unsteady mode.

## Grid Resolution

In an effort to better understand the effect of grid resolution on the flow field, the 14$^o$ angle of drift case was chosen. Two grids with identical surface resolutions, but varying field resolutions were generated. The coarse grid had moderate growth while the fine grid had interpolated growth [10]. The details of the two grids are summarized in Table 1. As can be seen from this table, the differences between the two grids are in the number of nodes and in the number of tetrahedra. This results from having more elements (predominantly tetrahedra) outside the “boundary layer” region.

The effect of the grid resolution on computed forces and moments is shown in Table 2. The coarse and fine grid computations are in good agreement with the experimental data, although the differences between the integrated quantities are not dramatic. The fine grid improves the axial force comparison, but degrades the pitching moment. Further interrogation of the computed flow fields is carried out by comparing contours of vorticity magnitude at an x/L = 0.98 (Figure 6). As can be seen, the extent of the high vorticity regions in the coarse grid solution

is significantly smaller than in the fine grid solution. Also noteworthy is absence of the secondary extremum in the coarse grid solution. The tip vortex is clearly visible in both the coarse and fine grid solutions. This particular location (x/L = 0.98) is representative of the differences that persist between the coarse and fine-grid flow fields.

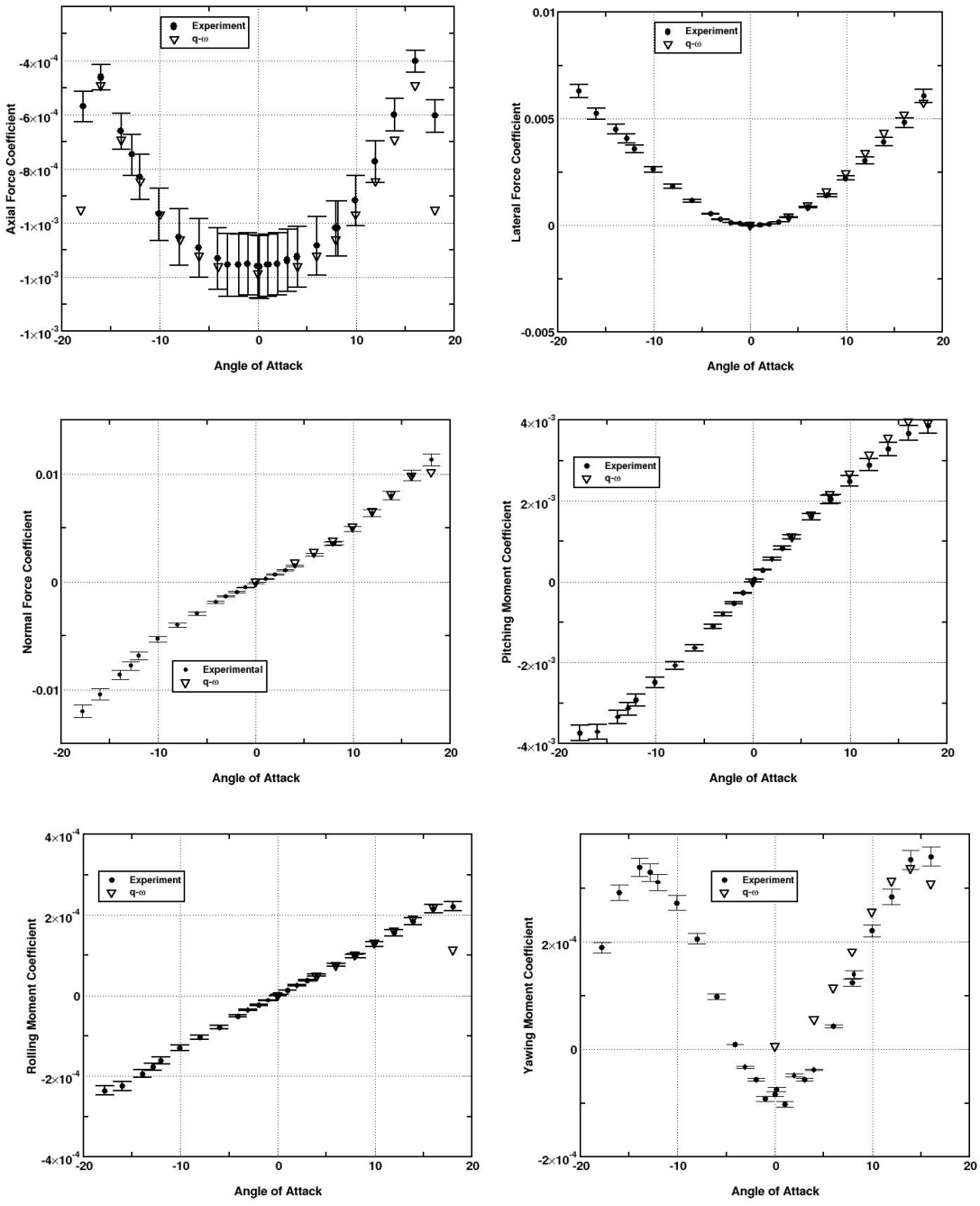


**Figure 5: Comparison of forces and moments for SUBOFF hull with sail**

**Table 1: Grid Statistics**

| Grid Type | Nodes | Tetrahedra | Pyramids | Prisms |
|---|---|---|---|---|
| Coarse | 3,019,307 | 5,873,471 | 6,491 | 3,920,255 |
| Fine | 3,879,007 | 10,967,299 | 6,495 | 3,920,251 |

**Table 2: Comparison of forces and moments for varying grid resolutions**

| Type | $F_x$ | $F_y$ | $F_z$ | $M_x$ | $M_y$ | $M_z$ |
|---|---|---|---|---|---|---|
| Experiment | -0.0006004 | 0.003919 | 0.00803 | 0.000184 | 0.0032820 | 0.0003527 |
| Coarse Grid | -0.0007139 | 0.004164 | 0.00793 | 0.000184 | 0.0035747 | 0.0003102 |
| Fine Grid | -0.0006843 | 0.004146 | 0.00794 | 0.000185 | 0.0035231 | 0.0002780 |

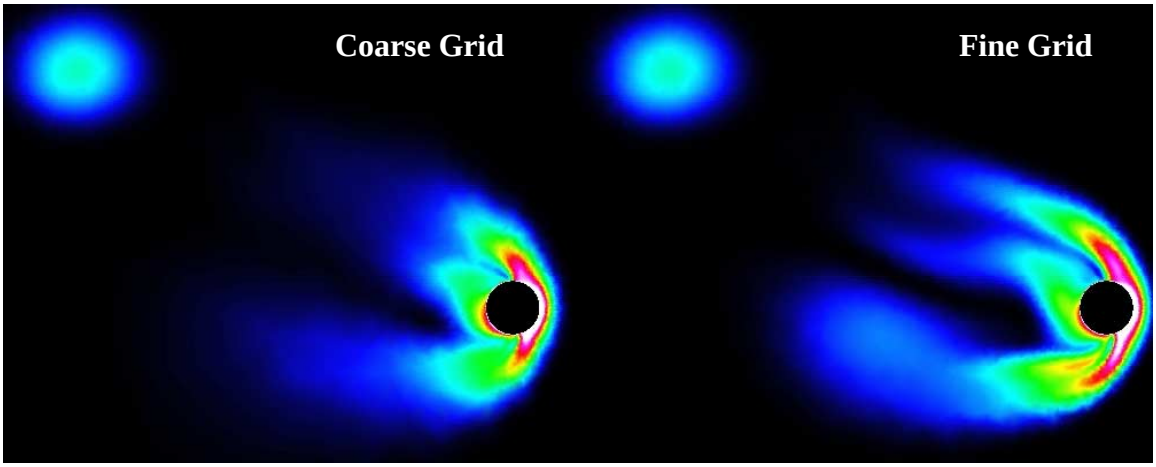


**Figure 6: Effect of grid resolution on vorticity magnitude (Model Scale)**

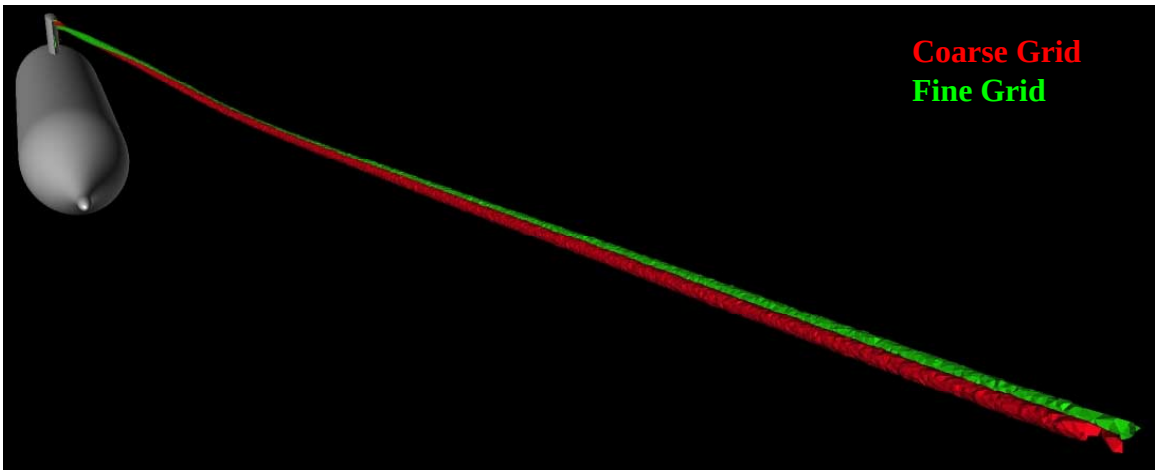


**Figure 7: Effect of grid resolution on tip vortex trajectory (Model Scale)**

Another manifestation of the effect of grid density can be observed by comparing the trajectories of the tip-vortex arising from the sail tip. The location of the tip-vortex is critical in determining the maneuvering and acoustic characteristics of a submarine. The coarse and fine grid trajectories are obtained by creating iso-surfaces of intrinsic swirl (iso-value = 1.5) and are shown in Figure 7. Two observations can be made: (a) The tip vortices persist for a significant distance downstream (b) Grid resolution is a fairly important player in predicting the vortex trajectory.

The sensitivity displayed by the model-scale computations lead the authors to build similar grids for the full-scale Reynolds numbers. The comparisons of vorticity magnitude at an x/L = 0.98 is presented in Figure 8. As can be seen from this figure, the full scale computations are fairly sensitive to field resolution. A comparison of tip vortex trajectory, determined using the iso-surface of intrinsic swirl (iso-value = 1.5), is shown in Figure 9.

Both model- and full-scale computations display significant sensitivity to field resolution. The features that get dissipated on the coarse grid are similar between the two cases. Further, there is significant similarity in the behavior of the tip vortices (coarse grid tip vortex being inboard compared to the fine grid tip vortex) between the model- and full-scale results.

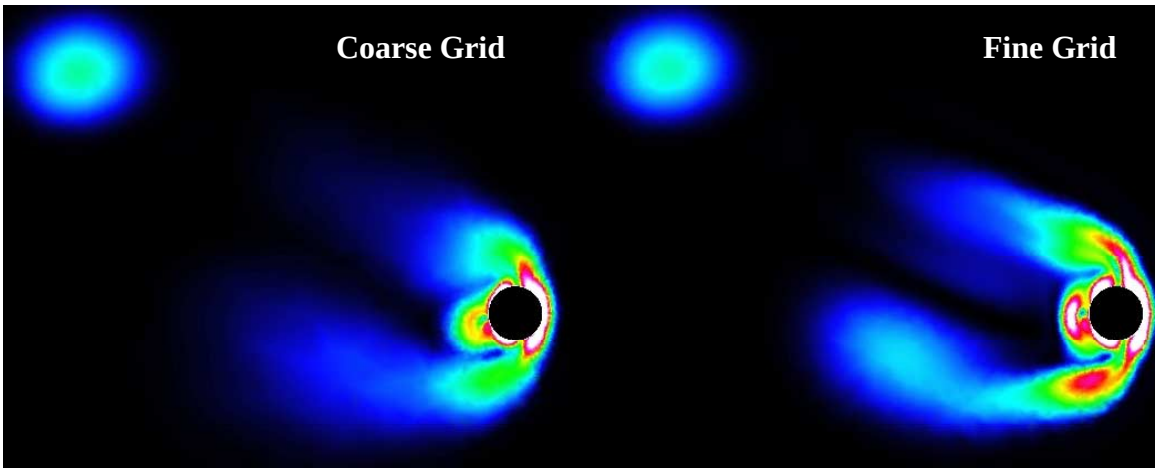


**Figure 8: Effect of grid resolution on vorticity magnitude (Full Scale)**

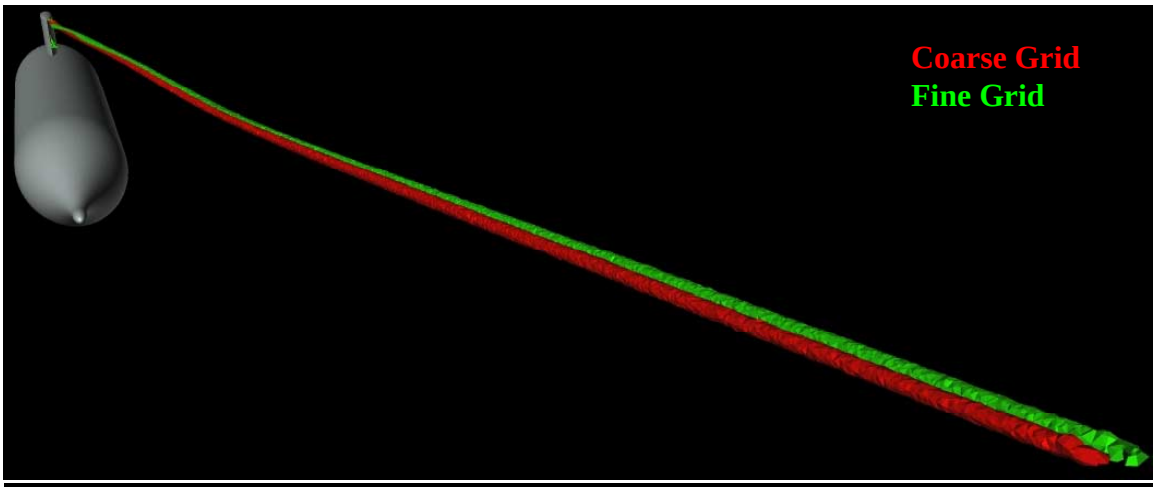


**Figure 9: Effect of grid resolution on tip vortex trajectory (Full Scale)**

## Scale Effects

In an effort to study the scale effects arising from an increase in Reynolds number, three cases were considered, i.e., model (Re = 14 million), quarter (Re = 250 million) and full (Re = 1000 million). All three cases were run at an angle of drift of $14^o$ and the maximum $y^+$ for all three cases was less than 1. Figure 10 shows the $y^+$ distribution on the surface of the SUBOFF model. $y^+$ essentially mimics the behavior of $C_f$, but does not get out of scale due to changes in Reynolds numbers. As can be seen from this figure, there are significant differences. The most striking ones are the differences in the strength of the separation lines around the sail-hull intersection. Also significant is the differences in the cross-flow separation with the full scale computations displaying the most clearly demarcated lines.

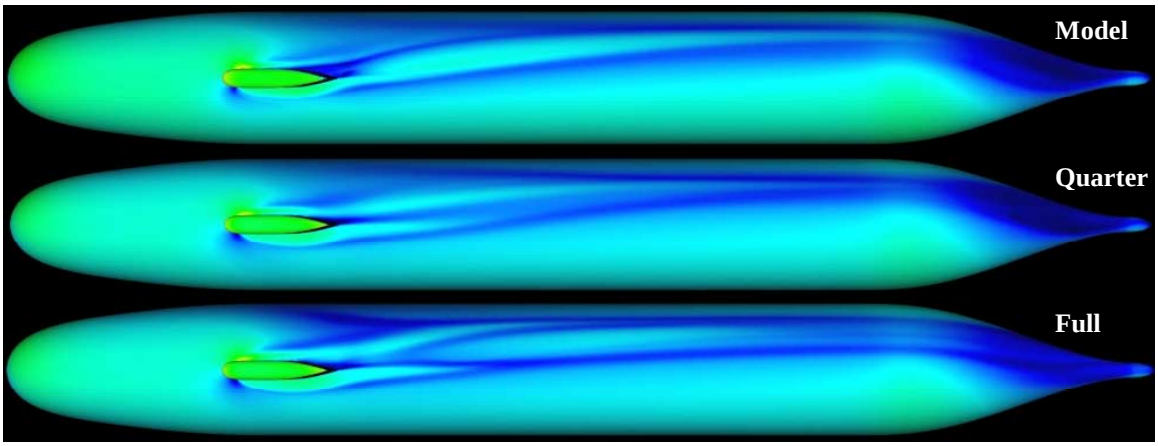


**Figure 10: Variation of $y^+$ distribution with Reynolds number**

Figures 11-13 show comparisons of vorticity contours between model-, quarter- and full-scale computations at various axial locations. The vorticity contours in all the figures are clipped to be within a range of zero (0) to 150 so that comparisons can be made across scales and axial locations. Figure 11 highlights the differences in the location and size of the horseshoe vortices at an axial location of 0.55. In the case of the model- scale, the horseshoe vortex can be seen very clearly, while in the full-scale results it lies significantly closer to the surface. The separation point on the lower half of the SUBOFF model is more sharply defined in the full-scale compared to the model-scale results. Clearly visible in all three cases is the tip vortex arising from the sail.

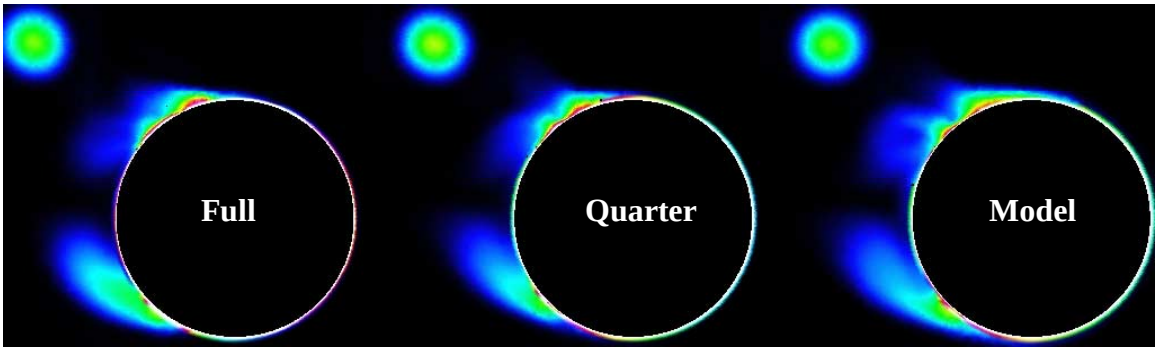


**Figure 11: Variation of vorticity with Reynolds Number (x/L = 0.55)**

A comparison of vorticity contours for an x/L of 0.98 is shown in Figure 12. As can be seen, there is an evolution of features as one transitions from model- to full-scale. Of specific interest is the evolution on the leeward side of the SUBOFF model. The region of high vorticity

that starts out as an amorphous blob at the model-scale becomes sharply defined as the Reynolds number is increased.

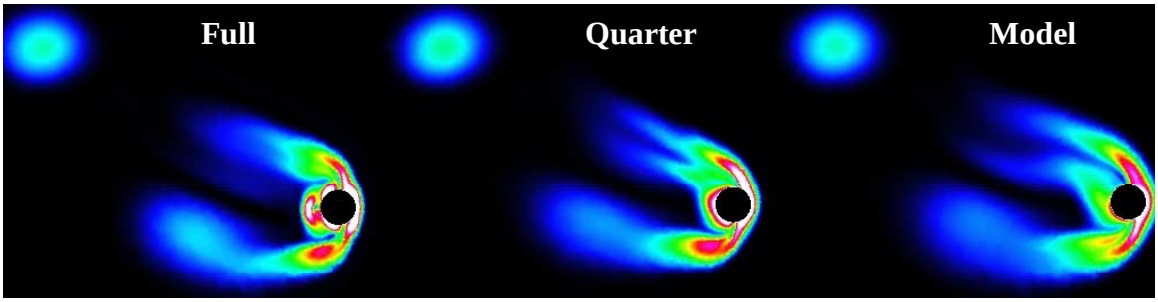


**Figure 12: Variation of vorticity with Reynolds number (x/L = 0.98)**

Figure 13 shows a comparison at a location downstream of the SUBOFF model (x/L = 1.3). The behavior at this location is similar to the one at an x/L = 0.98 in the sense that certain features that appear at model-scale coalesce (or sharpen) and strengthen as the Reynolds number is increased.

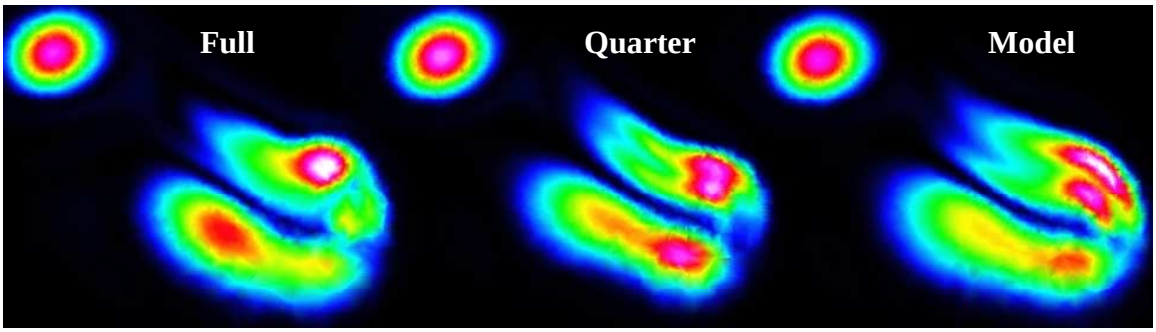


**Figure 13: Variation of vorticity with Reynolds number (x/L = 1.3)**

Significant differences can be seen between model-, quarter- and full-scale solutions. These differences are widespread and not localized to a specific location. Further, it is believed that these differences cannot be accounted for by a simple Reynolds number scaling.

## Conclusions

An attempt has been made to understand the role of grid resolution and scale effects on the solution for a notional submarine model. Further study is required to determine the optimal surface and volume resolutions that will yield better agreement with model-scale experimental data.

The ability to run quarter- and full-scale Reynolds numbers with good sub-layer resolution is considered a key feature of **U$^2$NCLE**. Results obtained during the course of this study show that simple Reynolds scaling probably will not account for the appearance of certain features at full-scale that are absent from the model-scale computations. Further validation of the quarter- and full-scale Reynolds number capabilities is required before any quantitative conclusions can be arrived at. Experimental data at a Reynolds number greater than model scale, perhaps at quarter- or even full-scale, would significantly assist in the validation process.

## Acknowledgements

This research was sponsored by the Office of Naval Research under grant number N00014-99-1-0751 with Dr. Patrick Purtell as technical monitor. This support is gratefully acknowledged.

## References

[1] Chorin, A.J., "A numerical method for solving incompressible viscous flow problems," *Journal of Computational Physics*, 2:12--26, 1967.

[2] Hyams, D.G., "An Investigation of Parallel Implicit Solution Algorithms for Incompressible Flows on Unstructured Topologies," Ph. D. Dissertation, Mississippi State University, May 2000.

[3] Berdahl, C.H., and Thompson, D.S., "Eduction of Swirling Structure Using the Velocity Gradient Tensor," *AIAA Journal*, Vol. 31, No. 1, January 1993.

[4] Remotigue, M.G., "Structured Grid Technology to Enable Flow Simulation in an Integrated System Environment," Ph. D. Dissertation, Mississippi State University, December 1999.

[5] Groves, N.C., Huang, T.T., and Chang, M.S., "Geometric characteristics of SUBOFF models," Technical Report DTRC/SHD-1298-01, David Taylor Research Center, Bethesda, Maryland, March 1989.

[6] Roddy, R.F., "Investigation of the stability and control characteristics of several configurations of the DARPA SUBOFF model from captive-model experiments," Technical Report DTRC/SHD-1298-08, David Taylor Research Center, Bethesda, Maryland, September 1990.

[7] Huang, T.T., Groves, N.C., Forlini, T.J., Blanton, J.N., and Gowing, S., "Measurement of flows over an axisymmetric body with various appendages," *Nineteenth Symposium on Naval Hydrodynamics*, South Korea, August 1992.

[8] Schlichting, H., *Boundary Layer Theory*, McGraw-Hill Book Company, Seventh edition, 1979.

[9] Hyams, D.G., Sreenivas, K., Sheng, C., Nichols, S., Taylor, L.K., Briley, W.R., Marcum, D.L., and Whitfield, D.L., "An Unstructured Multielement Solution Algorithm for Complex Geometry Hydrodynamic Simulations," 23rd Symposium of Naval Hydrodynamics, Val de Reuil, France, September 2000.

[10] SolidMesh Users Guide, "http://WWW.ERC.MsState.Edu/simcenter/docs/solidmesh"

**Paper: 29**
**Author: Dr. Sreenivas**

**Question by Dr. Khalid**: Your skin friction distribution comparisons do not show whether the experimental data are relevant to the full scale or the model scale results. You need to indicate that on the graph.

Answer: The experimental data was taken at model scale.

**Question by Dr. Watt**: Where is the image vortex to the sail tip vortex in your trailing vortex figures? Our experimental results show that a strong lower body separation vortex exists, even at moderate incidence angles.

Answer: Crossflow separation vortices exist at moderate to high angles of drift. They are not shown for clarity.

**Question by Mr. Mendenhall**: First I have a comment. It is not clear that Reynolds number effects have been demonstrated because similar size grids were not used, and your other results showed large grid effects.

What is the comparison for $C_N$ and $C_m$ between model and full scale?

Answer:

| Scale | $F_x$ | $F_y$ | $F_z$ | $M_x$ | $M_y$ | $M_z$ |
|---|---|---|---|---|---|---|
| Model | $6.8 \times 10^{-4}$ | $4.1 \times 10^{-3}$ | $7.9 \times 10^{-3}$ | $1.8 \times 10^{-4}$ | $3.5 \times 10^{-3}$ | $2.8 \times 10^{-4}$ |
| Full | $9.69 \times 10^{-5}$ | $3.9 \times 10^{-3}$ | $8 \times 10^{-3}$ | $1.8 \times 10^{-4}$ | $3.4 \times 10^{-3}$ | $2.6 \times 10^{-4}$ |

**Question by Dr. Pirzadeh**: In the fine grids, for the grid sensitivity study, where are the extra points distributed? Is the refinement achieved globally, or are extra nodes clustered in certain locations?

Answer: The extra grid points are distributed in the region outside the boundary layer.

**This page has been deliberately left blank**

---

**Page intentionnellement blanche**